THE JOURNAL OF PHYSICAL CHEMISTRY C
A JOURNAL OF THE AMERICAN CHEMICAL SOCIETY

pubs.acs.org/JPCC

Article

Chemical Nanoimaging and Characterizing Kinetics of Bimetallic Nanostructure-Plasmon-Driven Dimerization Reactions by Tip-Enhanced Raman Spectroscopy

Swati J. Patil and Dmitry Kurouski*

Cite This: https://doi.org/10.1021/acs.jpcc.3c06712

Read Online

ACCESS | Metrics & More | Article Recommendations | Supporting Information

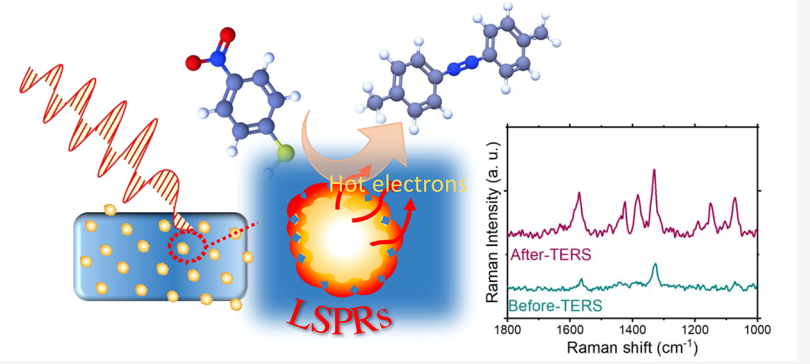

ABSTRACT: High synthetic costs of noble metal nanostructures, which are broadly used for plasmonic catalysis, triggered an interest in the use of less expensive metals such as copper for their fabrication. Catalytic properties of copper nanoparticles can be expanded by their doping with catalytic metals such as ruthenium or palladium. However, the catalytic properties of these novel bimetallic catalysts remain poorly understood. In this study, we used tip-enhanced Raman spectroscopy to investigate plasmon-driven transformation of 4-nitrobenzenethiol (4-NBT) to 4,4′-dimercaptoazobenzene (DMAB) on copper@ruthenium nanoparticles (Cu@RuNPs). We found that the presence of RuNPs on Cu nanoplate (CuNPt) surfaces drastically enhances catalytic reactivity of Cu@RuNPs compared to their monometallic analogues. The kinetics of the catalytic reaction have been studied, and the reaction rate constant for Cu@RuNPs is higher than that of CuNPts for hot-carrier-driven reduction of 4-NBT to DMAB. Our findings can be used to design novel bimetallic nanostructures with the desired catalytic properties.

INTRODUCTION

Plasmon-driven photocatalysis is based on the localized surface plasmon resonances (LSPRs)—coherent oscillations of conductive electrons on the metallic surfaces.[1−6] LSPRs are generated on the nanostructures by light and can decay producing heat or hot carriers, which are highly energetic species that drive the chemical transformation in molecules present on the metal surfaces.[7−12] For instance, noble metal nanostructures could catalyze O_2 and H_2 dissociation, reduction of 4-nitrobenzenethiol (4-NBT), and oxidation of 4-aminothiophenol (4-ATP) to *p*,*p*′-dimercaptoazobisbenzene (DMAB).[13−15]

High fabrication costs of noble metal nanostructures catalyze the search for less expensive metals.

Several research groups offered an elegant solution to this problem.[16−18] For instance, Halas's group showed that aluminum (Al) nanostructures could catalyze a large number of chemical reactions due to their strong LSPRs in visible and ultraviolet regions of the electromagnetic spectrum.[19,20] Linic's group discovered that copper nanoparticles (CuNPs) can be used to catalyze the conversion of propylene to propylene oxide.[21] The researchers found that CuNPs demonstrated a nearly 3 times higher selectivity compared to thermally driven catalysis.[21] In addition, Li and Kurouski demonstrated that Cu nanowires (CuNWs) and nanocubes (CuNCs) could be used to reduce 4-NBT to DMAB as well as 4-mercapto-phenylmethanol (4-MPM) to 4-mercaptobenzoic acid (4-MBA).[22]

Cu nanostructures can be also coupled with other materials such as semiconductors, metal−organic frameworks, or catalytic metals to expand their catalytic properties.[23−25] For instance, Ye and co-workers found that Cu/ZnO nanostructures could be used to reduce CO_2 into CH_3OH.[26] Atwater's

Received: October 9, 2023
Revised: December 11, 2023
Accepted: December 12, 2023

Downloaded via TEXAS A&M UNIV COLG STATION on January 3, 2024 at 21:21:00 (UTC).
See https://pubs.acs.org/sharingguidelines for options on how to legitimately share published articles.

© XXXX American Chemical Society

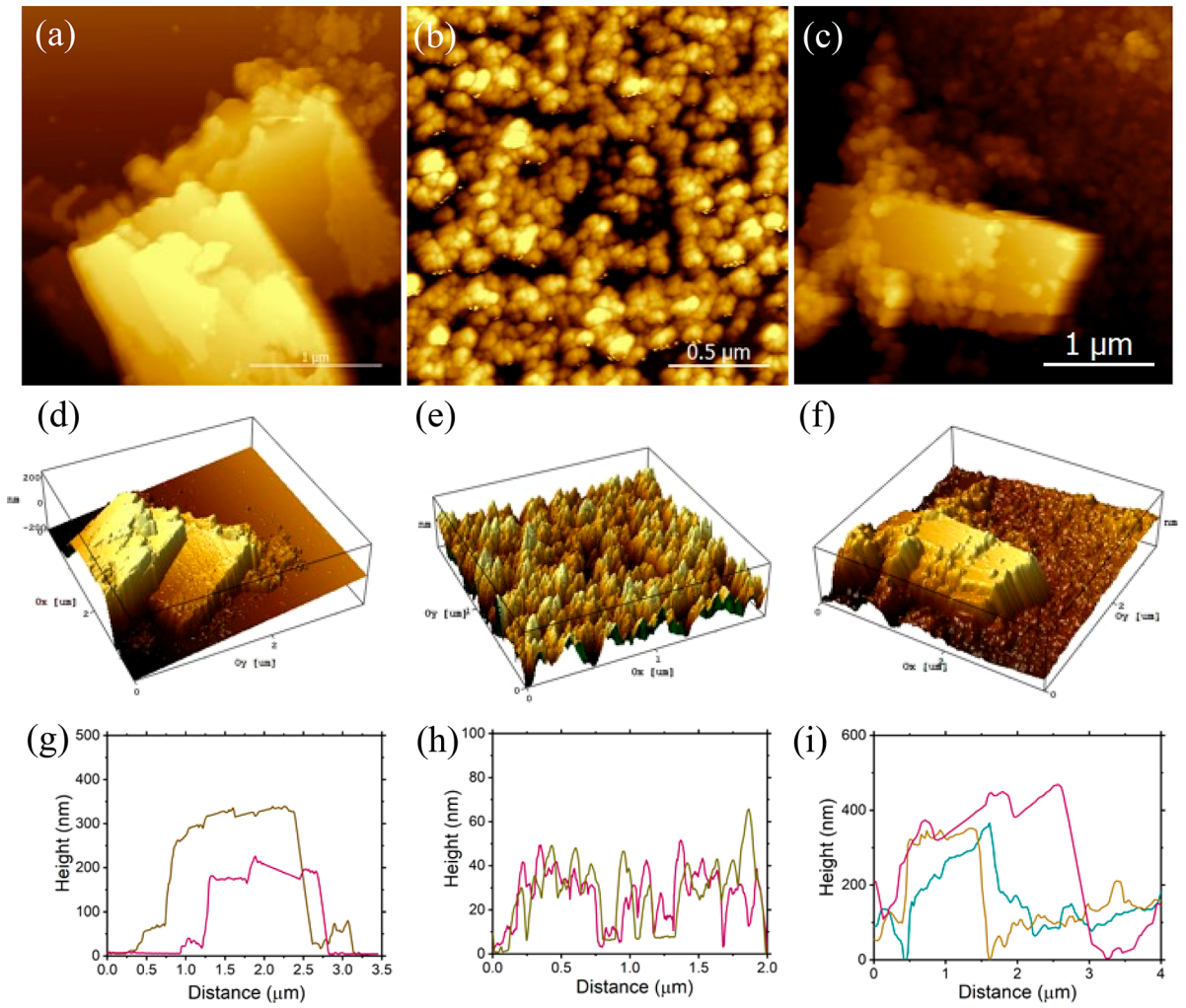

Figure 1. Topographical studies of CuNPts, RuNPs, and Cu@RuNPs: 2D and 3D AFM images of (a, d) Cu NPs, (b, e) RuNPs, and (c, f) Cu@RuNPs with the corresponding height profile of (g) CuNPts, (h) RuNPs, and (i) Cu@RuNPs.

group found that p-type nickel oxide (p-NiO) enhanced the catalytic efficiency of CuNPs, enabling a separation of hot carriers generated by the CuNPs.[27] These hot carriers then converted into a CO_2 anion that yielded CO, which in turn produced $HCOO^-$. Halas's group recently reported that Cu@Ru single-atom alloy nanoparticles were highly efficient and coke-resistant plasmonic photocatalysts for methane dry reforming.[18] The researchers also found that catalytic efficiency of these nanoparticles directly depends on the interplay between Cu and Ru atoms as well as the nanoscale architecture of these nanostructures. Among several precious metals, ruthenium (Ru) is a promising less expensive metal that has a high surface area and can effectively catalyze a wide range of reactions.[28] Specifically, it is an excellent oxidation catalyst in heterogeneous catalysis. Bimetallic catalysts that are precisely designed are one of the best ways to have a high impact on reactivity, better selectivity, and high stability. Alternatively, LSPR of Cu results in visible range absorption, which generates hot-electron excitations in metal and promotes charge transfer in heterogeneous nanoscale junctions.[29]

Tip-enhanced Raman spectroscopy (TERS) is a modern analytical approach that can be used to reveal plasmonic and photocatalytic properties of mono Cu nanoplates (CuNPts) and bimetallic Cu@RuNPs catalysts at the nanoscale.[30−32] In the current study, we use TERS to investigate plasmonic and photocatalytic properties of Cu@RuNPs at the nanoscale. Using 4-NBT as a molecular reporter, we determine the extent to which different surface sites of Cu@RuNPs and their monometallic analogues (CuNPts) were able to reduce this molecular analyte into DMAB.

EXPERIMENTAL METHODS

Chemicals. For this study, we used copper(II) chloride dihydrate ($CuCl_2{\cdot}2H_2O$), ruthenium(III) chloride hydrate ($RuCl_3{\cdot}xH_2O$), sodium borohydride ($NaBH_4$), polyvinylpyrrolidone (PVP), hexadecylamine (HAD), glucose, and ethanol (EtOH). All chemicals were obtained from Aldrich Chemical Co. and further used without any purification.

Cu@RuNPs Synthesis. Initially, Cu nanoplates (CuNPts) and nanocubes (CuNCs) were prepared as described in previous work published by Li et al.[23] The prepared nanoplates and nanocube solutions were centrifuged at 8000 rpm several times to remove impurities and byproducts with distilled water and ethanol. In the next step, the as-prepared CuNPts (50 mg) and $RuCl_3$ (3 mg) were dissolved in distilled water (20 mL) under continuous stirring at room temperature. Then, 1 mg of $NaBH_4$ was injected into the solution, and further PVP (0.2 g) was added as a stabilizer to avoid the agglomeration of RuNPs and kept stirring for 20 min. Within 12−15 min, the mixed

https://doi.org/10.1021/acs.jpcc.3c06712
J. Phys. Chem. C XXXX, XXX, XXX−XXX

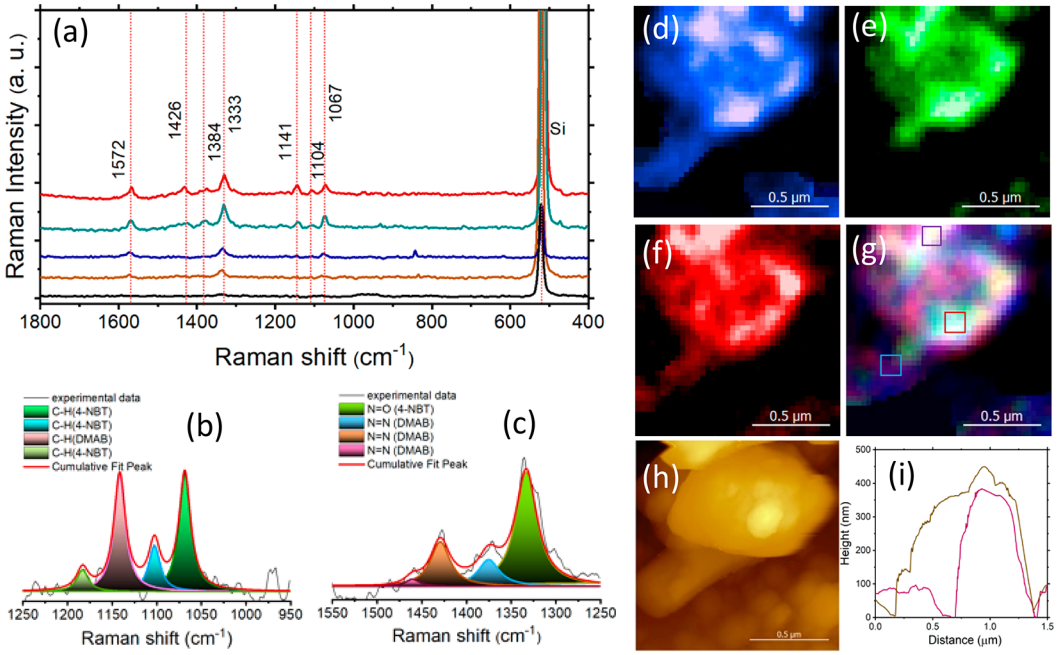

Figure 2. TERS imaging of plasmonic and photocatalytic properties of CuNPts. (a) TERS spectra were acquired from the surface of CuNPts coated with 4-NBT (color-coded in (g)). (b, c) Lorentz-fitted curves of the vibrational bands in the acquired TERS spectra that originated from 4-NBT and DMAB. TERS maps of 4-NBT at 1333 (d) and 1572 cm^{-1} (e) and of DMAB at 1384 and 1426 cm^{-1} (f), with the overlay of all three maps (g). (h) AFM image of CuNPts and their height profile (i). Scale bars are 0.5 μm.

solution color was changed from dark brown to reddish black, resulting in the reduction of Ru^{3+} to Ru^0. UV−vis spectroscopy was used to confirm Ru^{3+} reduction to Ru^0 (Figure S1).[34,35] After stirring, the solution was kept for 10 min for ultrasonication and then centrifuged at 10000 rpm with distilled water and ethanol 4−5 times.

Modification of the Monolayer of 4-NBT on Cu@RuNPs. A fresh silicon (Si) wafer (0.5 cm^2) was cleaned with acetone and ethanol and dried with nitrogen gas before use. A drop of the as-prepared CuNPts and Cu@RuNPs stock solution was first deposited on a precleaned Si wafer and dried at room temperature for 1 h. After 1 h, a monolayer of 2 mM 4-NBT ethanolic solutions was formed on CuNPts and Cu@RuNPs and kept for further drying for 1 h at room temperature. To remove uncoordinated molecules on the nanostructures, the modified sample was washed with ethanol multiple times and dried by nitrogen gas in the final step.

Preparation of TERS Probe. The commercially available silicon AFM probes were purchased from OPUS with the parameters of a 2 N/m force constant and resonance frequency of 70 kHz. Further, AFM probes were modified by coating them with a layer of gold (70 nm) by using metal evaporation (MBrown, Stratham, NH). The metal deposition parameters such as pressure were kept at ∼1 × 10^{-6} mbar and 0.1 Å/s deposition rate, and the deposition chamber temperature was 54 °C. After achieving 70 nm thickness of Au on the AFM tips, the evaporation was stopped and continued to cool to room temperature.

Instrumentation. The AIST-NT-HORIBA system was equipped with a 632.5 nm continuous-wavelength laser for AFM-TERS and AFM scanning. A 100× Mitutoyo microscope objective was used to bring laser light to the sample surface in side-illumination geometry. TERS maps were also collected with the same objective and directed introduced to a fiber-coupled Horiba iHR550 spectrograph equipped with a Synapse EM-CCD camera (Horiba, Edison, NJ). The surface microstructures of the prepared samples were captured by using a JEOL JSM-7500F- field emission scanning electron microscope (FE-SEM) equipped with a high brightness conical FE gun and a low aberration conical objective lens.

RESULTS AND DISCUSSION

First, we utilized atomic force microscopy to examine the topography of Cu@RuNPs, CuNPts, and ruthenium nanoparticles (RuNPs) (Figure 1). The fabricated Cu NPs had a height of 350 ± 2 nm, whereas RuNPs were 30 ± 2 nm in diameter, as shown in Figure 1a,b. Cu@RuNPs exhibited a high density of RuNPs on their surfaces with well-defined boundaries between CuNPts and RuNPs (Figure 1c). We used UV−vis spectroscopy to determine the optical properties of the developed nanomaterials (Figure S1). We found that CuNPts exhibited an absorption maximum ∼635 nm that was broadened and red-shifted as a result of CuNPts decoration with RuNPs.[33,34] In addition, FE-SEM images of the CuNPt and Cu@RuNPs are demonstrated in Figure S4, evidence of nanostructure of the prepared materials.

In Figure 2, TERS imaging was used to examine catalytic properties of CuNPts with a monolayer of 4-NBT on their surfaces. The TERS spectrum of 4-NBT exhibited distinct vibrational bands at 1067, 1104, 1333, 1384, 1426, and 1572 cm^{-1}. Vibrational bands at 1067, 1333, and 1572 cm^{-1} correspond to C−H bending modes, NO symmetric stretching, and the ring C═C stretching vibration of 4-NBT, respectively.[35,36] Moreover, the vibrational band at 1104 and 1141 cm^{-1} was attributed to δ(C−H) for 4-NBT and DMAB, respectively.[37] TERS revealed the formation of DMAB on the surfaces of CuNPts. This conclusion could be made by the observation of N═N vibrations (1384 and 1426 cm^{-1}) in the acquired TERS spectra (Figure 2b,c).[38] TERS imaging reveals a high distribution of DMAB on the surface of Cu NPs (Figure

https://doi.org/10.1021/acs.jpcc.3c06712
J. Phys. Chem. C XXXX, XXX, XXX−XXX

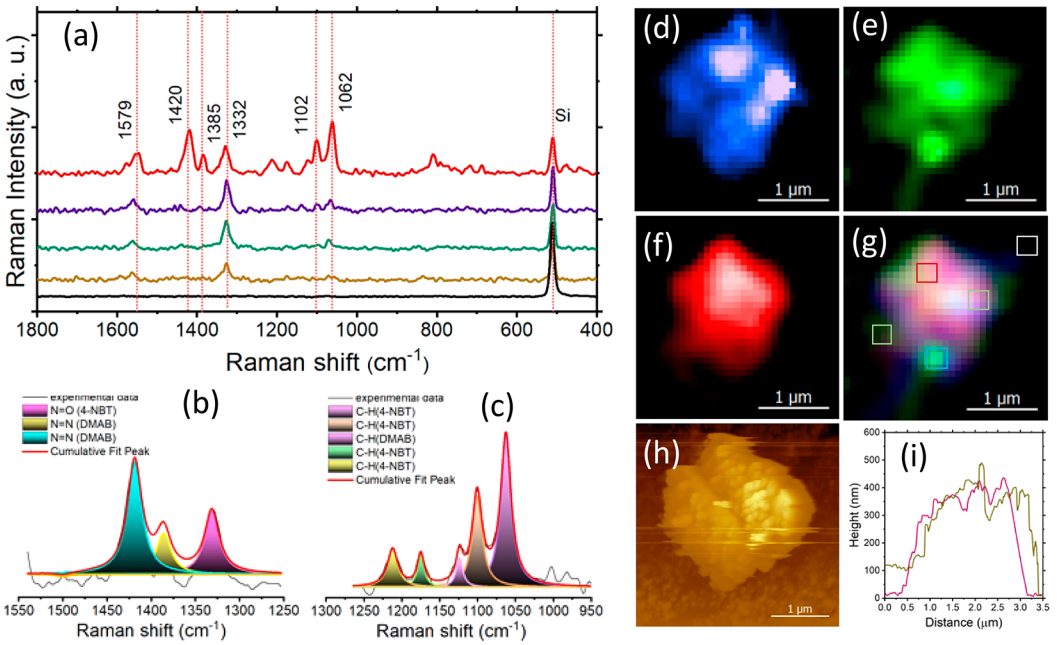

Figure 3. TERS imaging of plasmonic and photocatalytic properties of Cu@RuNPs. (a) TERS spectra were acquired from the surface of Cu@RuNPs coated with 4-NBT (color-coded in (g)). (b, c) Lorentz-fitted curves of the vibrational bands in the acquired TERS spectra that originated from 4-NBT and DMAB. TERS maps of 4-NBT at 1332 cm^{-1} (d) and 1579 cm^{-1} (e) and of DMAB at 1385 and 1420 cm^{-1} (f), with the overlay of all three maps (g). (h) AFM image of Cu@RuNPs and their height profile (i). Scale bars are 0.5 μm.

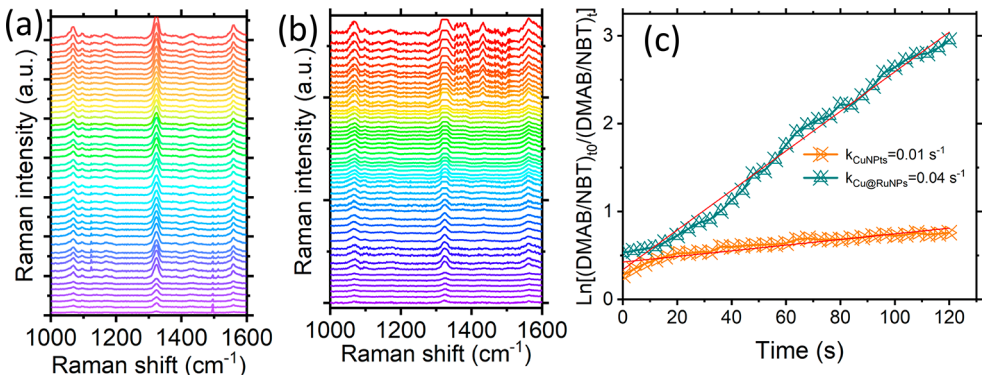

Figure 4. TERS kinetic measurements of 4-NBT to DMAB reduction on (a) CuNPts and (b) Cu@RuNPs at different reaction times. (c) Based on the intensity ratio of the bands 1425 cm^{-1} (DMAB) to 1333 cm^{-1} (4-NBT) in TERS spectra, rate constants of 4-NBT to DMAB reduction were calculated.

2f). The assessing reactivity distribution of 0.32 further calculated considering the ratio of DMAB/NBT. These findings demonstrated that unlike CuNWs and CuNCs which demonstrated a great yield of DMAB at their edges and corners,[22] the entire surface area of CuNPts was highly reactive.

Next, we performed TERS imaging of Cu@RuNPs with the monolayer of 4-NBT on their surfaces (Figures 3 and S3). We found that Cu@RuNPs were able to dimerize 4-NBT into DMAB (Figure 3a–c). We also found that some surface sites of Cu@RuNPs were far more reactive than others (Figure 3d–g). Although no direct correlation with the topography of Cu@RuNPs was observed, we infer that sites with a high catalytic reactivity could be occupied with RuNPs. We also found substantial differences in the intensity of N═O (1332 cm^{-1}) and C═C (1579 cm^{-1}) bands in the spectra acquired from Cu@RuNPs. In our previous study, we demonstrated that the ratio between these two bands directly depended on the orientation of 4-NBT on the metallic surfaces.[39] Thus, we can conclude that 4-NBT had drastically different orientations on the surfaces of Cu and Ru metals present in Cu@RuNPs.

Figure 4 shows the kinetic studies for the reduction of 4-NBT to DMAB on CuNPts and Cu@RuNPs. The intensity of the typical 4-NBT band at 1333 cm^{-1}, which is attributed to $(NO)_2$, in comparison to the intensity of the DMAB band at 1425 cm^{-1}, was utilized for quantification to measure the reaction over time. By measuring the change in intensities between 1425 cm^{-1} (DMAB) and 1333 cm^{-1} (4-NBT), we plotted a natural logarithm of their ratio at different reaction times using the equation[40,41]

$$\ln\left[\frac{(4\text{-}NBT)_{t=0}}{(4\text{-}NBT)_t}\right] = \ln\left[\frac{(I_{1425}/I_{1333})_{t=0}}{(I_{1425}/I_{1333})_t}\right] = kt \quad (1)$$

where $4\text{-}NBT_{t=0}$ and $4\text{-}NBT_t$ are the concentration at initial and final reaction times, respectively. The intensities of the bands DMAB at 1425 cm^{-1} and 4-NBT at 1333 cm^{-1} are

https://doi.org/10.1021/acs.jpcc.3c06712
J. Phys. Chem. C XXXX, XXX, XXX−XXX

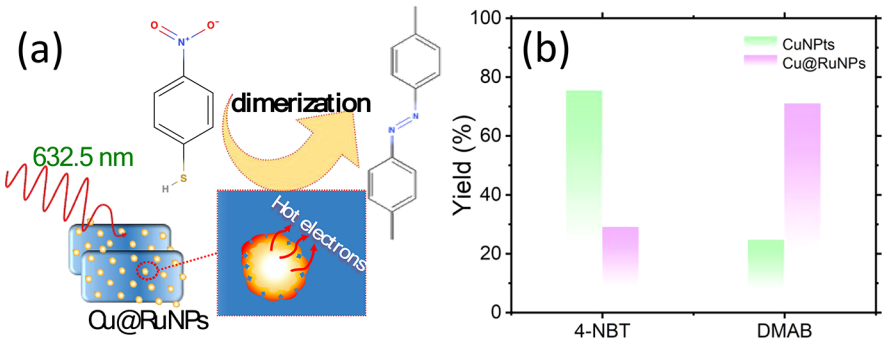

Figure 5. (a) Schematic illustration of the plasmon-driven surface-catalyzed reaction of 4-NBT on the Cu@RuNPs. (b) Histogram of the calculated yield of DMAB on CuNPts and Cu@RuNPs.

denoted by I_{1425} and I_{1333}, respectively. The rate constant is k, and the reaction time is t. It has been observed that after 80 s of reaction time, the rate constant of the reactions catalyzed marginally decreased in both cases. The rate constant for CuNPts and Cu@RuNPs is 0.01 and 0.04 s^{-1}, respectively, which are calculated from Figure 4c by linear fitting the data curve. These results indicate that Cu@RuNPs has a higher hot-carrier-driven reduction rate of 4-NBT to DMAB than CuNPts.

A schematic illustration for the plasmon-driven catalyzed reaction on Cu@RuNPs is shown in Figure 5a. Finally, we calculated the number of TERS spectra that exhibit the vibrational signature of DMAB on both CuNPts and Cu@RuNPs, as shown in Figure 5b. Based on these results, we can conclude that the presence of Ru drastically increased the catalytic reactions of CuNPts. One can expect that molecular orientation in addition to the high catalytic properties of Ru can contribute to the substantially greater yield of DMAB on Cu@RuNPs compared to CuNPts.

CONCLUSIONS

TERS imaging revealed that both CuNPts and Cu@RuNPs were capable of performing plasmon-driven reduction of 4-NBT into DMAB. We also found that unlike CuNWs and CuNCs, the entire surface of CuNPts was found to be catalytically active. Our results also showed that the presence of Ru drastically altered the plasmonic and photocatalytic properties of CuNPts. Specifically, RuNPs on Cu@RuNPs altered the orientation of 4-NBT and drastically increased the yield of DMAB. These findings open new avenues for the improvement of the catalytic properties of nanomaterials.

ASSOCIATED CONTENT

Supporting Information

The Supporting Information is available free of charge at https://pubs.acs.org/doi/10.1021/acs.jpcc.3c06712.

UV−vis spectra acquired from CuNPts, Cu@RuNPs, Ru(II), and Ru^0; TERS imaging of plasmonic and photocatalytic properties of CuNPt and Cu@RuNPs together with FE-SEM images of the (a) CuNPt and (b) Cu@RuNPs (PDF)

AUTHOR INFORMATION

Corresponding Author

Dmitry Kurouski − *Department of Biochemistry and Biophysics and Department of Biomedical Engineering, Texas A&M University, College Station, Texas 77843, United States;* orcid.org/0000-0002-6040-4213; Email: dkurouski@tamu.edu

Author

Swati J. Patil − *Department of Biochemistry and Biophysics, Texas A&M University, College Station, Texas 77843, United States;* orcid.org/0000-0002-3619-2783

Complete contact information is available at: https://pubs.acs.org/10.1021/acs.jpcc.3c06712

Notes

The authors declare no competing financial interest.

ACKNOWLEDGMENTS

We are grateful to AgriLife Research of Texas A&M for financial support. We also acknowledge the Governor's University Research Initiative (GURI) grant program of Texas A&M University, GURI Grant Agreement No. 12-2016, M1700437.

REFERENCES

(1) Kleinman, S. L.; Frontiera, R. R.; Henry, A. I.; Dieringer, J. A.; Van Duyne, R. P. Creating, Characterizing, and Controlling Chemistry with SERS Hot Spots. *Phys. Chem. Chem. Phys.* **2013**, *15* (1), 21−36.

(2) Brown, R. J. C.; Milton, M. J. T. Nanostructures and Nanostructured Substrates for Surface-Enhanced Raman Scattering (SERS). *J. Raman Spectrosc.* **2008**, *39* (10), 1313−1326.

(3) Moskovits, M. Surface Roughness and the Enhanced Intensity of Raman Scattering by Molecules Adsorbed on Metals. *J. Chem. Phys.* **1978**, *69* (9), 4159−4161.

(4) Gersten, J.; Nitzan, A. Electromagnetic Theory of Enhanced Raman Scattering by Molecules Adsorbed on Rough Surfaces. *J. Chem. Phys.* **1980**, *73* (7), 3023−3027.

(5) Kerker, M.; Wang, D.-S.; Chew, H. Surface Enhanced Raman Scattering (SERS) by Molecules Adsorbed at Spherical Particles: Errata. *Appl. Opt.* **1980**, *19* (24), 4159.

(6) King, F. W.; Van Duyne, R. P.; Schatz, G. C. Theory of Raman Scattering by Molecules Adsorbed on Electrode Surfaces. *J. Chem. Phys.* **1978**, *69* (10), 4472−4481.

(7) Cortés, E.; Xie, W.; Cambiasso, J.; Jermyn, A. S.; Sundararaman, R.; Narang, P.; Schlücker, S.; Maier, S. A. Plasmonic Hot Electron Transport Drives Nano-Localized Chemistry. *Nat. Commun.* **2017**, *8*, 1−10.

(8) Brown, A. M.; Sundararaman, R.; Narang, P.; Goddard, W. A.; Atwater, H. A. Nonradiative Plasmon Decay and Hot Carrier Dynamics: Effects of Phonons, Surfaces, and Geometry. *ACS Nano* **2016**, *10* (1), 957−966.

(9) Brongersma, M. L.; Halas, N. J.; Nordlander, P. Plasmon-Induced Hot Carrier Science and Technology. *Nat. Nanotechnol.* **2015**, *10* (1), 25−34.
(10) Lauchner, A.; Schlather, A. E.; Manjavacas, A.; Cui, Y.; McClain, M. J.; Stec, G. J.; García De Abajo, F. J.; Nordlander, P.; Halas, N. J. Molecular Plasmonics. *Nano Lett.* **2015**, *15* (9), 6208−6214.
(11) Zhou, L.; et al. Aluminum Nanocrystals as a Plasmonic Photocatalyst for Hydrogen Dissociation. *Nano Lett.* **2016**, *16* (2), 1478−1484.
(12) Ma, J.; Wang, Z.; Wang, L. W. Interplay between Plasmon and Single-Particle Excitations in a Metal Nanocluster. *Nat. Commun.* **2015**, *6* (5), 10107.
(13) Huang, Y. F.; Zhu, H. P.; Liu, G. K.; Wu, D. Y.; Ren, B.; Tian, Z. Q. When the Signal Is Not from the Original Molecule to Be Detected: Chemical Transformation of Para-Aminothiophenol on Ag during the SERS Measurement. *J. Am. Chem. Soc.* **2010**, *132* (27), 9244−9246.
(14) Huang, Y.-F.; Wu, D.-Y.; Zhu, H.-P.; Zhao, L.-B.; Liu, G.-K.; Ren, B.; Tian, Z.-Q. Surface-Enhanced Raman Spectroscopic Study of p-Aminothiophenol. *Phys. Chem. Chem. Phys.* **2012**, *14* (24), 8485−8497.
(15) Mukherjee, S.; et al. Hot Electrons Do the Impossible: Plasmon-Induced Dissociation of H2 on Au. *Nano Lett.* **2013**, *13*, 240−247.
(16) Mukherjee, S.; Zhou, L.; Goodman, A. M.; Large, N.; Ayala-Orozco, C.; Zhang, Y.; Nordlander, P.; Halas, N. J. Hot-Electron-Induced Dissociation of H2 on Gold Nanoparticles Supported on SiO_2. *J. Am. Chem. Soc.* **2014**, *136* (1), 64−67.
(17) Swearer, D. F.; Robatjazi, H.; Martirez, J. M. P.; Zhang, M.; Zhou, L.; Carter, E. A.; Nordlander, P.; Halas, N. J. Plasmonic Photocatalysis of Nitrous Oxide into N2 and O2 Using Aluminum-Iridium Antenna-Reactor Nanoparticles. *ACS Nano* **2019**, *13* (7), 8076−8086.
(18) Zhou, L.; et al. Light-Driven Methane Dry Reforming with Single Atomic Site Antenna-Reactor Plasmonic Photocatalysts. *Nat. Energy* **2020**, *5* (1), 61−70.
(19) Knight, M. W.; King, N. S.; Liu, L.; Everitt, H. O.; Nordlander, P.; Halas, N. J. Aluminum for Plasmonics. *ACS Nano* **2014**, *8* (1), 834−840.
(20) Jacobson, C. R.; Solti, D.; Renard, D.; Yuan, L.; Lou, M.; Halas, N. J. Shining Light on Aluminum Nanoparticle Synthesis. *Acc. Chem. Res.* **2020**, *53* (9), 2020−2030.
(21) Marimuthu, A.; Zhang, J.; Linic, S. Tuning Selectivity in Propylene Epoxidation by Plasmon Mediated Photo-Switching of Cu Oxidation State. *Science (80-.)* **2013**, *339* (6127), 1590−1593.
(22) Li, Z.; Kurouski, D. Tip-Enhanced Raman Analysis of Plasmonic and Photocatalytic Properties of Copper Nanomaterials. *J. Phys. Chem. Lett.* **2021**, *12* (34), 8335−8340.
(23) Xin, Y.; Yu, K.; Zhang, L.; Yang, Y.; Yuan, H.; Li, H.; Wang, L.; Zeng, J. Copper-Based Plasmonic Catalysis: Recent Advances and Future Perspectives. *Adv. Mater.* **2021**, *33* (32), 1−26.
(24) Li, X.; Wang, Y.; Yin, C.; Yin, Z. Copper Nanowires in Recent Electronic Applications: Progress and Perspectives. *J. Mater. Chem. C* **2020**, *8* (3), 849−872.
(25) Gawande, M. B.; Goswami, A.; Felpin, F. X.; Asefa, T.; Huang, X.; Silva, R.; Zou, X.; Zboril, R.; Varma, R. S. Cu and Cu-Based Nanoparticles: Synthesis and Applications in Catalysis. *Chem. Rev.* **2016**, *116* (6), 3722−3811.
(26) Wang, Z.; et al. Photo-Assisted Methanol Synthesis via CO_2 Reduction under Ambient Pressure over Plasmonic Cu/ZnO Catalysts. *Appl. Catal. B Environ.* **2019**, *250* (February), 10−16.
(27) Duchene, J. S.; Tagliabue, G.; Welch, A. J.; Li, X.; Cheng, W. H.; Atwater, H. A. Optical Excitation of a Nanoparticle Cu/p-NiO Photocathode Improves Reaction Selectivity for CO_2 Reduction in Aqueous Electrolytes. *Nano Lett.* **2020**, *20* (4), 2348−2358.
(28) Axet, M. R.; Philippot, K. Catalysis with Colloidal Ruthenium Nanoparticles. *Chem. Rev.* **2020**, *120* (2), 1085−1145.
(29) Kowalska, E.; Yoshiiri, K.; Wei, Z.; Zheng, S.; Kastl, E.; Remita, H.; Ohtani, B.; Rau, S. Hybrid Photocatalysts Composed of Titania Modified with Plasmonic Nanoparticles and Ruthenium Complexes for Decomposition of Organic Compounds. *Appl. Catal. B Environ.* **2015**, *178*, 133−143.
(30) Li, Z.; Wang, R.; Kurouski, D. Nanoscale Photocatalytic Activity of Gold and Gold-Palladium Nanostructures Revealed by Tip-Enhanced Raman Spectroscopy. *J. Phys. Chem. Lett.* **2020**, *11* (14), 5531−5537.
(31) Li, Z.; Rigor, J.; Large, N.; El-Khoury, P. Z.; Kurouski, D. Underlying Mechanisms of Hot Carrier-Driven Reactivity on Bimetallic Nanostructures. *J. Phys. Chem. C* **2021**, *125* (4), 2492−2501.
(32) Li, Z.; Kurouski, D. Plasmon-Driven Chemistry on Mono- And Bimetallic Nanostructures. *Acc. Chem. Res.* **2021**, *54* (10), 2477−2487.
(33) Burda, C.; Chen, X.; Narayanan, R.; El-Sayed, M. A. Chemistry and Properties of Nanocrystals of Different Shapes. *Chem. Rev.* **2005**, *105* (4), 1025−1102.
(34) Linic, S.; Christopher, P.; Ingram, D. B. Plasmonic-Metal Nanostructures for Efficient Conversion of Solar to Chemical Energy. *Nat. Mater.* **2011**, *10* (12), 911−921.
(35) Li, Z.; Kurouski, D. Elucidation of Photocatalytic Properties of Gold-Platinum Bimetallic Nanoplates Using Tip-Enhanced Raman Spectroscopy. *J. Phys. Chem. C* **2020**, *124* (23), 12850−12854.
(36) Wang, R.; Kurouski, D. Elucidation of Tip-Broadening Effect in Tip-Enhanced Raman Spectroscopy (TERS): A Cause of Artifacts or Potential for 3D TERS. *J. Phys. Chem. C* **2018**, *122* (42), 24334−24340.
(37) Li, Z.; Kurouski, D. Probing the Redox Selectivity on Au@Pd and Au@Pt Bimetallic Nanoplates by Tip-Enhanced Raman Spectroscopy. *ACS Photonics* **2021**, *8* (7), 2112−2119.
(38) Liu, Y.; et al. A Study of Plasmon-Driven Catalytic 4-NBT to DMAB in the Dry Film by Using Spatial Raman Mapping Spectroscopy. *Nano Res.* **2022**, *15* (7), 6062−6066.
(39) Li, Z.; El-Khoury, P. Z.; Kurouski, D. Tip-Enhanced Raman Imaging of Photocatalytic Reactions on Thermally-Reshaped Gold and Gold-Palladium Microplates. *Chem. Commun.* **2021**, *57* (7), 891−894.
(40) Li, Z.; Wang, R.; Kurouski, D. Nanoscale Photocatalytic Activity of Gold and Gold-Palladium Nanostructures Revealed by Tip-Enhanced Raman Spectroscopy. *J. Phys. Chem. Lett.* **2020**, *11* (14), 5531−5537.
(41) Joseph, V.; Engelbrekt, C.; Zhang, J.; Gernert, U.; Ulstrup, J.; Kneipp, J. Characterizing the Kinetics of Nanoparticle-Catalyzed Reactions by Surface-Enhanced Raman Scattering. *Angew. Chemie - Int. Ed.* **2012**, *51* (30), 7592−7596.

https://doi.org/10.1021/acs.jpcc.3c06712
J. Phys. Chem. C XXXX, XXX, XXX−XXX